Gain of a High-Impedance Cavity Coupled to Strongly Driven Semiconductor Quantum Dots

Si-Si Gu,[1,2] Yong-Qiang Xu,[1,2] Rui Wu,[1,2] Shun-Li Jiang,[1,2] Shu-Kun Ye,[1,2] Ting Lin,[1,2] Bao-Chuan Wang,[1,2] Hai-Ou Li,[1,2,3] Gang Cao,[1,2,3,*] and Guo-Ping Guo[1,2,3,4]

[1] *CAS Key Laboratory of Quantum Information, University of Science and Technology of China, Hefei, Anhui 230026, China*

[2] *CAS Center for Excellence in Quantum Information and Quantum Physics, University of Science and Technology of China, Hefei, Anhui 230026, China*

[3] *Hefei National Laboratory, University of Science and Technology of China, Hefei 230088, China*

[4] *Origin Quantum Computing Company Limited, Hefei, Anhui 230088, China*

(Received 25 November 2022; revised 17 February 2023; accepted 31 March 2023; published 5 May 2023)

The architecture of artificial atoms coupled to superconducting cavities allows the study of light-matter interactions and intriguing phenomena such as cavity gain implying photon generation. Here, we integrate a high-impedance cavity with a double quantum dot (DQD) in GaAs/(Al,Ga)As heterostructures, achieving a considerable DQD-cavity coupling strength and a relatively small cavity decay rate. By applying a strong drive to the DQD, we realize a population inversion and observe the cavity amplitude gain in multiple regions in the measured Landau-Zener-Stückelberg-Majorana interference pattern. We further systematically investigate the dependence of cavity gain on the driving frequency and tunnel coupling strength of the DQD. The results show that the cavity gain is tunable, with a maximum value of approximately 1.16 in the measured range. Our experimental results are in good agreement with theoretical simulations and may provide an opportunity to implement on-chip microwave sources or microwave amplifiers in a controllable way.

DOI: 10.1103/PhysRevApplied.19.054020

I. INTRODUCTION

The integration of artificial atoms with superconducting cavities in circuit quantum electrodynamics (QED) architecture provides a platform to study light-matter interactions at the quantum level [1–3]. Recent progress in strong qubit-cavity coupling [4–12], photon-mediated coherent coupling between distant qubits [13–19], and cavity-based readout of the qubit states [4,20,21] opens up a way to scalable quantum networks [22] and wide implementations in quantum information processing [2,3,23]. In addition, harnessing the light-matter interaction, artificial atoms can play the role of the gain medium, making it possible to engineer cavity fields and generate cavity photons [3,24].

Gate-defined semiconductor quantum dot (QD) is one of the versatile and ideal artificial atoms due to the high tunability of energy-level structure [25,26] and the underlying rich physics [2,27–29]. Many works have demonstrated a cavity gain in QD-based circuit QED setup [30–34], which suggests photon generation. On one hand, experiments have applied source-drain bias to a double QD (DQD) to generate population inversion, achieving an obvious cavity amplitude gain [30,34], photon emission [30,35], and even lasing [31,32]. On the other hand, by applying a continuous microwave to the DQD, the Landau-Zener-Stückelberg-Majorana (LZSM) interference [36] and the assistance of electron-phonon interactions in the InAs material lead to population inversion [33,37], hence a more controllable way for photon generation has been realized in an InAs nanowire DQD embedded in a cavity [33].

However, for a more scalable strongly driven DQD defined in heterostructures, the cavity amplitude gain is hindered by the insufficient DQD-cavity coupling strength [38]. In contrast to QDs in InAs nanowires, buried quantum wells in heterostructures constrain the distance between QDs and cavities, which limits the DQD-cavity coupling strength. Recent advances in high-impedance superconducting cavities have greatly improved the DQD-cavity coupling strength [7,9,11], offering the possibility of visible cavity gain.

In this paper, we couple a high-impedance superconducting Nb-Ti-N cavity to a GaAs DQD in a circuit QED setup. The DQD is periodically driven with a continuous microwave, leading to an effective population inversion of the Floquet states [33,37] with the help of the electron-phonon interactions in GaAs. Benefiting from the good

*gcao@ustc.edu.cn

performance of the cavity, we observe cavity amplitude gain in multiple regions of the LZSM pattern. We further study the influence of the drive and the DQD parameters on the cavity gain in detail. By varying driving frequency v_d and interdot tunnel coupling $2t$, we tune the cavity gain and obtain a maximum value of approximately 1.16.

II. EXPERIMENTAL SETUP

Our device [Fig. 1(a)] consists of two DQDs and a half-wavelength ($\lambda/2$) transmission microwave cavity, but only one DQD marked with an orange rectangle is used in the experiment. The DQD is formed on a GaAs/(Al, Ga)As heterostructure with the confinement potential electrically tuned by gate electrodes [Fig. 1(b)]. The source and the drain are grounded. An excess electron in the DQD occupying the left or right dot defines a charge qubit in a basis spanned by $|L\rangle = (m+1, n)$ and $|R\rangle = (m, n+1)$, where (m, n) denotes the number of electrons in two dots. In this basis, the Hamiltonian is given by $H_{\rm DQD} = (\epsilon\sigma_z + 2t\sigma_x)/2$, where σ_x and σ_z are the Pauli matrices. ϵ is the detuning between $|L\rangle$ and $|R\rangle$, and $2t$ is the interdot tunnel coupling. We control ϵ ($2t$) using the gate voltages $V_{\rm BR}$ ($V_{\rm MU}$ and $V_{\rm MD}$). The DQD's transition frequency is $f_q = \sqrt{\epsilon^2 + 4t^2}/h$, where h is Planck's constant.

To couple with the cavity, the plunger gate of the DQD [pink in Fig. 1(b)] is galvanically connected to a voltage antinode of the cavity. Our cavity is fabricated from an 11-nm-thick Nb-Ti-N film with a narrow cavity center conductor (approximately 320 nm) to achieve a high characteristic impedance ($Z_r \sim 2$ kΩ) [9,39], resulting in enhanced coupling strength g between the DQD and the cavity ($g \propto \sqrt{Z_r}$) [7,11]. The cavity has a center frequency $f_c = 5.196$ GHz and decay rate $\kappa/2\pi = 11.2$ MHz.

In the experiment, the device is cooled in a dilution refrigerator with a base temperature of approximately 17 mK. To read out the charge states of the DQD, we apply a probe microwave into the cavity at the frequency $f_p = f_c$ and measure the transmission signal by a vector network analyzer. Figure 1(c) shows the measured normalized cavity transmission amplitude A/A_0 as a function of gate voltages $V_{\rm BR}$ and $V_{\rm BL}$, which exhibits the charge-stability diagram of the DQD. A_0 is the averaged cavity transmission amplitude with the DQD in the Coulomb blockade regime [8,33]. Fitting the data with the input-output theory [6,40], we estimate the coupling strength $g/2\pi \approx 56$ MHz and the DQD's decoherence rate $\gamma/2\pi \approx 100$ MHz at $2t/h \approx 5.3$ GHz.

III. CAVITY AMPLITUDE GAIN

We drive the DQD by applying a continuous microwave at frequency v_d and amplitude A_d to gate BR. Therefore, the detuning is modulated as $\epsilon = \epsilon_0 + A_d \cos(2\pi v_d t)$ with the offset detuning ϵ_0. A/A_0 shows the LZSM pattern as a function of ϵ_0 and driving power $P_d \propto A_d^2$ in Fig. 2(a). In general, only loss stripes ($A/A_0 < 1$) appear for a transmission cavity when the probe frequency is fixed at $f_p = f_c$ [38,41]. Interestingly, a series of cavity amplitude gain ($A/A_0 > 1$) stripes are observed besides the loss stripes. Within the measured range, several regions marked by green rectangles display similar gain magnitudes. We denote them as G1, G2, and G3, with the driving power from low to high for simplicity. The cavity gain indicates that the DQD transfers energy to the cavity by emitting photons into the cavity mode [30,33,37].

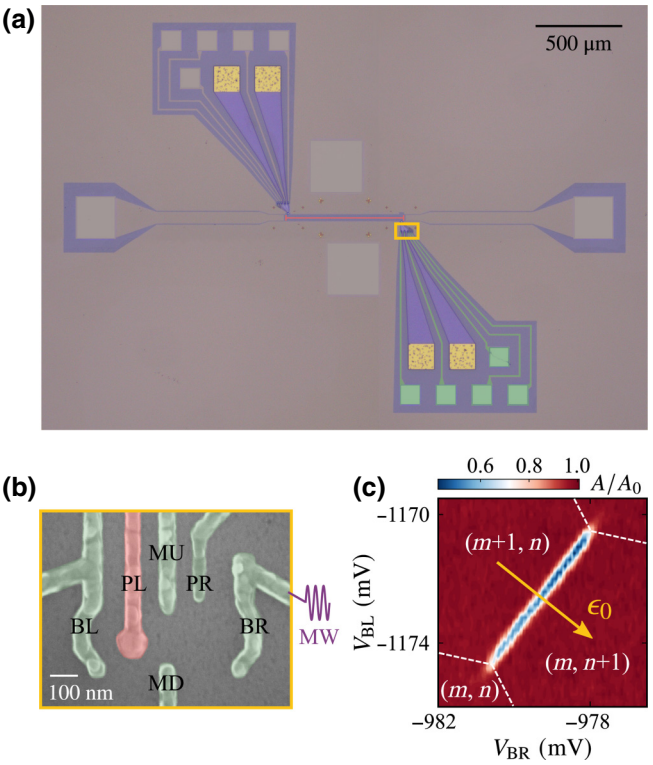

FIG. 1. (a) False-color optical micrograph of the hybrid system composed of two DQDs and a superconducting Nb-Ti-N transmission cavity. (b) False-color scanning electron micrograph of the DQD. Gate electrodes BL, PL, MU, PR, BR, and MD are used to define a double-well potential for the DQD. The plunger gate PL (pink) is connected to the cavity. (c) The charge-stability diagram of the DQD extracted from normalized cavity transmission A/A_0.

The Floquet theory [43], which provides a powerful tool to describe the dynamics of periodically driven systems, can be used to understand the origin of the photon emission. In this theory, the solution of the time-dependent Schrödinger equation is expressed as $|\psi_\alpha(t)\rangle = e^{-i\mu_\alpha t/h}|\phi_\alpha(t)\rangle$ ($\alpha = 0, 1$), where $|\phi_\alpha(t)\rangle$ is the Floquet state with its quasienergy μ_α. As the Floquet state keeps the same periodicity as the drive, $|\phi_\alpha(t)\rangle = |\phi_\alpha(t + 1/v_d)\rangle$, it can be Fourier decomposed as $|\phi_\alpha(t)\rangle = \sum_k e^{-i2\pi k v_d t}|\phi_{\alpha,k}\rangle$ with an integer k. $|\phi_{\alpha,k}\rangle$ is the kth Fourier component of $|\phi_\alpha(t)\rangle$ with its quasienergy shifted,

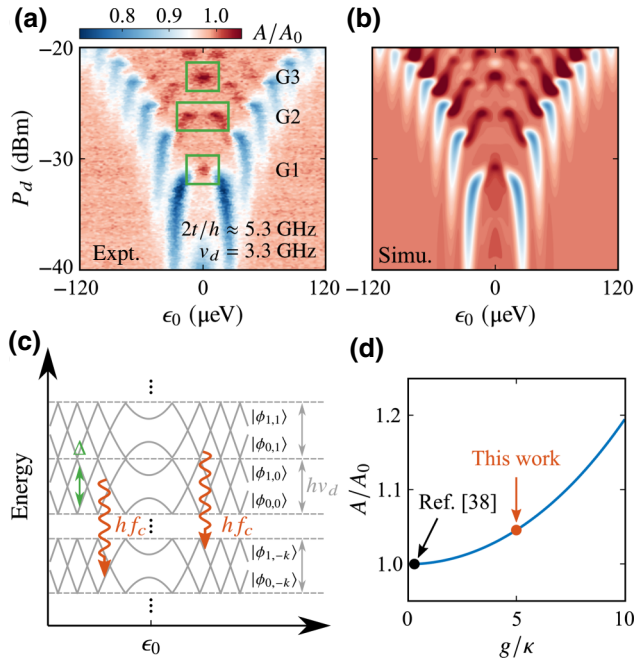

FIG. 2. (a) The LZSM interference pattern obtained by measuring A/A_0 at driving frequency $v_d = 3.3$ GHz and $2t/h \approx 5.3$ GHz. The maximum gain is about 1.07. (b) The corresponding theoretical simulation results, see details for theory in Appendix. B. The driving power $P_d = -40$ dBm corresponds to amplitude $A_d = 11.4$ μeV in the simulation. We consider the fluctuations of the detuning ϵ and the driving amplitude A_d by convoluting all the theoretical plots with a Gaussian distribution of width $\sigma_\epsilon = 3.3$ μeV along the ϵ axis and $\sigma_{P_d} = 0.2$ dBm along the P_d axis [33,41,42]. (c) Schematic diagram of the quasienergy spectrum of the Floquet states, which repeats with the period hv_d. Red arrows indicate the case in which the energy splitting of two levels matches the cavity frequency and a photon is emitted into the cavity. (d) The theoretical calculated A/A_0 at G1 as a function of the ratio g/κ.

$\mu_{\alpha,k} = \mu_\alpha + khv_d$. Therefore, the Floquet quasienergy spectrum has a Brillouin zone structure with a periodic width equal to the energy quantum of hv_d, which is schematically illustrated in Fig. 2(c). The quasienergy is modulated by the detuning ϵ_0, since the quasienergy can be understood as the combined energy of the DQD and the driving field with $\mu_\alpha(\epsilon_0, 2t, A_d, v_d)$.

Analogous to the analysis in Ref. [33], the competition between the drive-assisted phonon relaxation and bare phonon relaxation contributes to a larger excited Floquet state population, generating a population inversion in the Floquet basis. As the driving frequency $v_d < f_c$ in this experiment, the relevant Floquet states are in different Brillouin zones in contrast to Ref. [33]. Moreover, when the quasienergy difference of these two states is on resonance with the cavity, i.e., $\Delta + hkv_d = hf_c$ or $h(k+1)v_d - \Delta = hf_c$, the driven DQD emits a photon into the cavity as indicated by the red arrows in Fig. 2(c). Here, $\Delta = \mu_1 - \mu_0$ is the splitting of two quasienergy levels within a Brillouin zone (the green arrow). In this framework, the relaxation processes and the quasienergy difference are modulated by the system parameters. Therefore, the observed A/A_0 shows oscillatory behavior in Fig. 2(a). The simulation result obtained with Floquet theory is shown in Fig. 2(b) and is in good agreement with the data, quantitatively confirming our analysis.

Given that the population inversion and resonance conditions give rise to photon emission, it is natural that the emission rate depends on the DQD-cavity coupling strength g. However, this process competes with the cavity photon decay at rate κ due to the coupling of the cavity to the environment. Consequently, to observe the cavity gain, a large coupling strength g and a small cavity decay rate κ are necessary. This is illustrated with the theoretical prediction in Fig. 2(d), the cavity amplitude at G1 decreases as the ratio g/κ becomes smaller. When $g/\kappa < 1$, A/A_0 is close to 1. As recently demonstrated on a transmission cavity containing a similar driven GaAs DQD [38], only loss stripes appear because of the small g and large κ ($g/\kappa \approx 0.3$, the black point). In contrast, our device has been improved by enhancing g with a high-impedance cavity and suppressing the cavity decay with an optimized fabrication process to reach $g/\kappa \approx 5.0$ (the red point), contributing to the visible cavity gain.

IV. THE INFLUENCE OF DRIVING FREQUENCY AND TUNNEL COUPLING STRENGTH

We demonstrate that the preceding measurement results can be interpreted by the competition between photon emission and photon loss. To get more insight into the cavity gain, its dependence on system parameters is investigated. In this section, we show that the photon emission process is tunable by driving frequency v_d and tunnel coupling $2t$.

First, we study the influence of v_d on the cavity gain. Figures 3(a)–3(c) show the evolution of the LZSM patterns for different driving frequencies $v_d = 3.2, 3.35, 3.5$ GHz while fixing $2t/h \approx 5.3$ GHz. At $v_d = 3.2$ GHz, the cavity gain at G3 is slightly larger than that at G1 and G2. As v_d increases to 3.35 GHz, cavity gains are comparable at three regions and the largest at G2. When $v_d = 3.5$ GHz, the cavity gain at G1 is the largest. To obtain a complete dependence of the cavity gain on v_d, we change v_d from 3.15 to 3.7 GHz in steps of 50 MHz and measure the LZSM interference patterns at every v_d. As the LZSM patterns are similar to Figs. 3(a)–3(c) except that the gain value changed, these patterns are not shown here for brevity. The extracted gain values at G1 to G3 are plotted in Figs. 3(d)–3(f), respectively. We find the same trend of the gain at three regions, increasing and then decreasing over the measured v_d range.

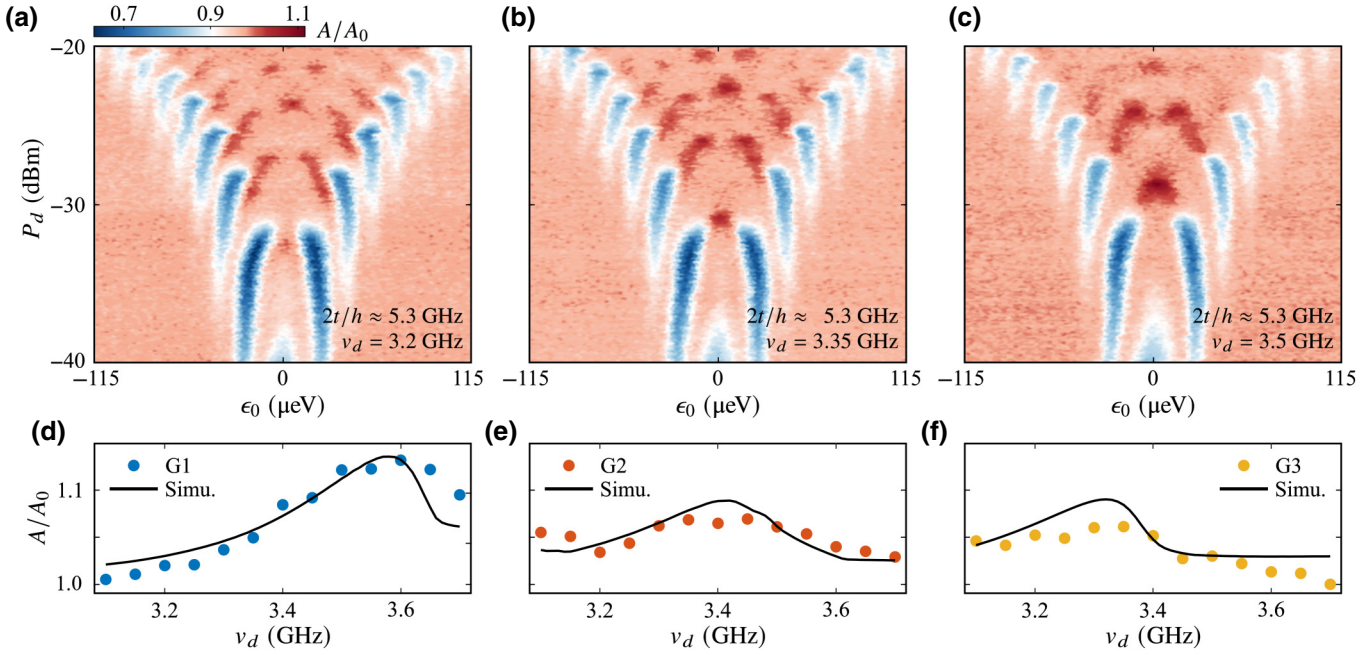

FIG. 3. The A/A_0 as a function of ϵ_0 and P_d at driving frequency (a) $v_d = 3.2$ GHz, (b) $v_d = 3.35$ GHz, (c) $v_d = 3.5$ GHz. The maximum A/A_0 at (d) G1, (e) G2, (f) G3 extracted from LZSM patterns as a function of v_d (dots) and the corresponding simulation results (solid lines). The simulated maximum A/A_0 at G1–G3 are extracted from the calculated LZSM interference patterns as the positions of G1–G3 vary with v_d.

The tunability of A/A_0 by v_d can be qualitatively understood by considering the population distribution, quasienergy μ_α, and the effective coupling strength g_{eff} between the Floquet states and the cavity [see Eqs. (B7) and (B8) in the Appendix]. v_d affects the drive-assisted phonon relaxation process, leading to a change in the effective population of the Floquet states. Meanwhile, the fulfillment of the resonance conditions is modulated by v_d since μ_α is a function of v_d. And g_{eff} is a function of driving and DQD parameters as $g_{\text{eff}}(v_d, 2t)$ [44]. Thus, all these ingredients contribute to a variation of the gain. Another observed feature, the maximum cavity gain of approximately 1.13 is reached at G1 with $v_d = 3.6$ GHz rather than at G2 and G3, is probably due to a larger g_{eff} at G1 compared to that at G2 and G3 [44]. All the features are well captured by the theoretical calculation results, as shown by the solid lines in Figs. 3(d)–3(f).

We now investigate the dependence of the cavity gain on $2t$. At each $2t$, the equivalent experiments as in Fig. 3 are performed by varying v_d. And the extracted cavity gain at G1 to G3 is similarly plotted as a function of v_d, see Appendix C. We see that at different $2t$, the maximum cavity gain value is always obtained at G1 instead of at G2 or G3, consistent with the observation in Fig. 3 and owing to a larger effective coupling at G1 [44]. Furthermore, at each $2t$, we record the maximum cavity gain and the corresponding applied driving frequency, denoted as the optimal driving frequency v_d^{opt}. Figure 4(a) displays v_d^{opt} as a function of $2t$, where v_d^{opt} increases as the transition frequency of the DQD becomes larger. The maximum cavity gain as a function of $2t$ is plotted in Fig. 4(b). Overall, we find a larger cavity gain for increased $2t$, with the largest $A/A_0 \approx 1.16$ reached at $2t/h \approx 6.2$ GHz and $v_d = 3.775$ GHz within the measured parameters.

The $2t$ dependence of the maximum A/A_0 can be interpreted similarly to v_d. The variation of $2t$ affects μ_α,

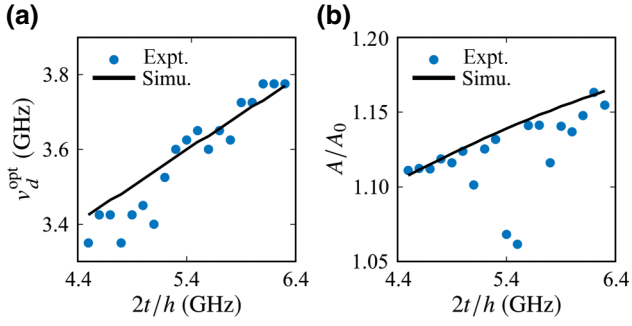

FIG. 4. (a) The optimal driving frequency v_d^{opt} and (b) the maximum cavity gain as a function of $2t/h$. At different $2t$, we vary v_d and extract the cavity gain from the LZSM interference patterns, which is plotted as a function of v_d in Appendix. C. From this, the optimal driving frequency and maximum cavity gain at each $2t$ are determined. The solid lines are the calculated theoretical results obtained with the same method as in Fig. 3.

thereby modulating the phonon relaxation process and the fulfillment of the resonance conditions. And as mentioned above, g_{eff} is a function of $2t$. Therefore, the tunability of gain by $2t$ is also a result of multiple factors. The theoretical simulations for v_d^{opt} and the maximum A/A_0 as a function of $2t$ (the solid lines in Fig. 4) are in good agreement with the experimental data. However, some measured maximum A/A_0 deviates from the simulation, which is not completely understood and warrants further investigation.

V. CONCLUSION AND OUTLOOK

In conclusion, we realize a population inversion of Floquet states in a strongly driven DQD formed on a GaAs/(Al,Ga)As heterosturcture. Taking advantage of the cavity's high impedance and improved quality, the appreciable coupling strength g between the DQD and the cavity as well as the relatively small cavity decay rate κ facilitate the observation of cavity amplitude gain ($A/A_0 > 1$). We observe that multiple regions in the LZSM pattern display amplitude gain, implying that the DQD emits photons into the cavity. Furthermore, the dependence of the cavity gain on driving frequency v_d and tunnel coupling $2t$ is measured, demonstrating the tunability of the photon emission process.

The cavity gain can be further enhanced by optimizing the cavity with higher quality and impedance as predicted by theory. Improving the cavity design [19] and substituting the cavity materials with higher inductance material such as TiN [45] and granular aluminum [46,47] allow a further increase in cavity impedance and achieve a larger g. In addition, it is possible to reduce cavity loss with microwave engineering like on-chip microwave filters [48–50] and the optimized fabrication process [51]. With all the improvements, we expect the investigation of photon statistics with correlation function measurement [52,53] and the achievement of microwave sources and amplifiers in a controllable way [37]. Our scheme is general and transferable to QD systems hosted on other semiconductor material, such as silicon. Moreover, this kind of tunable hybrid system is convenient to integrate with other qubits on the same chip and can work at low temperature [54], which offers broad application prospects.

ACKNOWLEDGMENTS

This work is supported by the National Natural Science Foundation of China (Grants No. 61922074, No. 92265113, No. 12074368, and No. 12034018) and the Innovation Program for Quantum Science and Technology (Grant No. 2021ZD0302300). This work is partially carried out at the University of Science and Technology of China Center for Micro and Nanoscale Research and Fabrication.

APPENDIX A: MEASUREMENT SETUP

The device is cooled using a cryogen-free dilution refrigerator, and the circuit diagram of the measurement setup is shown in Fig. 5. The cavity probe tone is generated by a vector network analyzer (VNA) and attenuated about 76 dB before arriving at the cavity port. The cavity output signal is amplified by HEMT at 4 K and two amplifiers at room temperature sequentially, finally measured by the VNA. The microwave drive is generated by a microwave source and reaches the BR gate through a bias tee.

APPENDIX B: THEORY

In this section, we introduce the theory [55] employed for the simulation.

1. Floquet theory

The DQD with a periodic drive is described by a time-dependent Hamiltonian,

$$H_{\text{DQD}} = \frac{1}{2}[(\epsilon_0 + A_d \sin(2\pi v_d t))\sigma_z + 2t\sigma_x]. \tag{B1}$$

A_d (v_d) is the amplitude (frequency) of the driving microwave. And $2t$ is the interdot tunnel coupling. σ_x and σ_z are the Pauli operators for the DQD.

Thus, the Schrödinger equation is

$$\left(-i\hbar\frac{d}{dt} + H_{\text{DQD}}\right)|\psi(t)\rangle = 0, \tag{B2}$$

which can be solved with Floquet theory [43].

The set of solutions to the Schrödinger equation can be expressed in the form:

$$|\psi_\alpha(t)\rangle = e^{-i\mu_\alpha t/\hbar}|\phi_\alpha(t)\rangle, \tag{B3}$$

where $|\phi_\alpha(t)\rangle$ is the Floquet state and μ_α is the corresponding quasienergy. $|\phi_\alpha(t)\rangle$ has the same periodicity as the drive, which can be expanded into the Fourier-series representation as $|\phi_\alpha(t)\rangle = \sum_{k=-\infty}^{\infty} e^{-i2\pi k v_d t}|\phi_{\alpha,k}\rangle$ with an integer k, and $|\phi_{\alpha,k}\rangle$ is the kth Fourier component of $|\phi_\alpha(t)\rangle$.

By expressing the above Eq. (B2) in the Fourier-series representation, a time-independent equation can be obtained [56]. Note that this transformation is realized at the cost of the infinite state space, but we can numerically solve the time-independent equation with appropriate truncation.

2. Floquet-Bloch-Redfield theory

When the system dissipation is weak [57], the stationary state of the driven DQD system is diagonal in the Floquet basis as $\rho(t) = \sum_\alpha p_\alpha |\phi_\alpha(t)\rangle\langle\phi_\alpha(t)|$. p_α is the occupation probability of the Floquet state $|\phi_\alpha(t)\rangle$, which can be

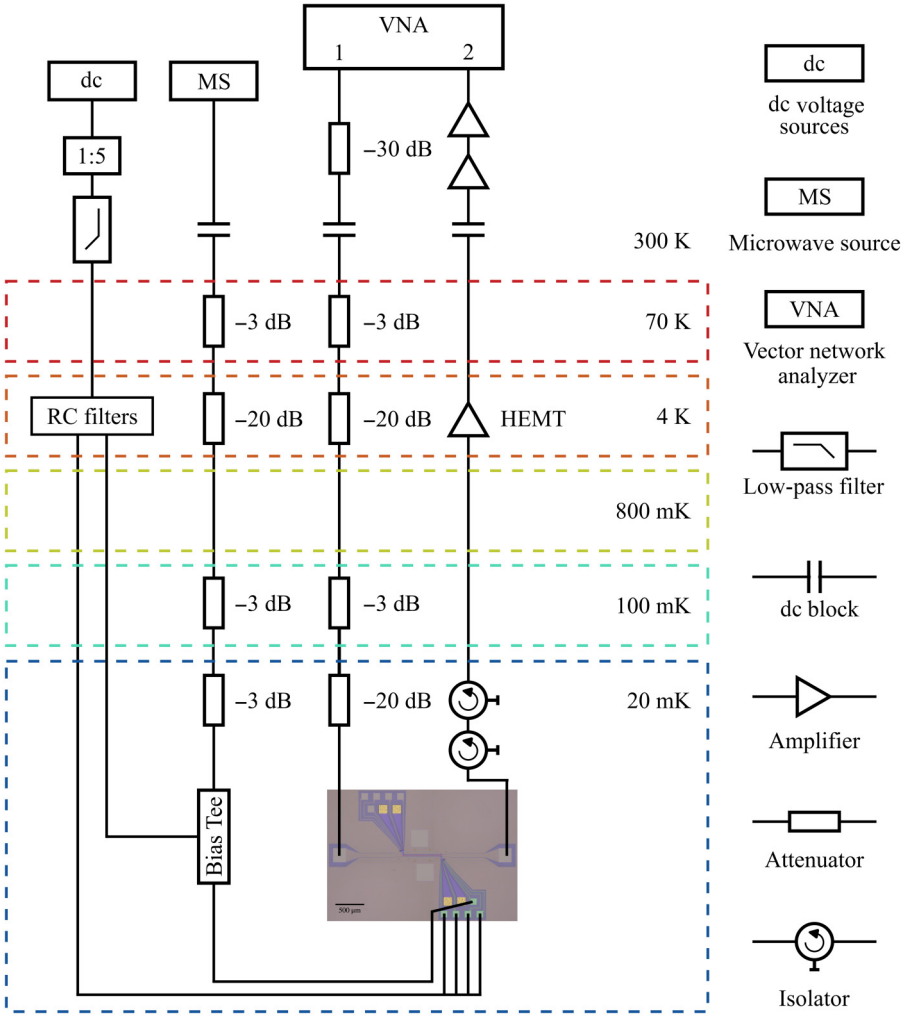

FIG. 5. Schematic of the measurement setup.

obtained with the Floquet-Bloch-Redfield theory [55,57]. It follows the master equation as

$$\dot{p_\alpha} = \sum_\beta (w_{\alpha\leftarrow\beta} p_\beta - w_{\beta\leftarrow\alpha} p_\alpha), \tag{B4}$$

where $w_{\alpha\leftarrow\beta}$ is the transition rate from state $|\phi_\beta(t)\rangle$ to state $|\phi_\alpha(t)\rangle$.

To consider the transition due to the electron-phonon interactions [55,58], a system-bath model is introduced:

$$H_{\text{el-ph}} = X \sum_v \lambda_v (b_v^\dagger + b_v) + \sum_v \omega_v b_v^\dagger b_v, \tag{B5}$$

where ω_v is the frequency of the vth phonon and $b_v^\dagger(b_v)$ is the phonon creation (annihilation) operator. λ_v is the coupling between the DQD and phonon. Here, we choose $X = \sigma_x$ [42,55]. With this Hamiltonian, the transition rate derived from the electron-phonon interactions can be expressed as

$$w_{\alpha\leftarrow\beta} = 2 \sum_k |\sum_{k'} \langle \phi_{\alpha,k'+k} | \sigma_z | \phi_{\beta,k'} \rangle|^2 \times N(\mu_\alpha - \mu_\beta + k\Omega), \tag{B6}$$

where $N(\omega) = J(\omega) n_{\text{th}}(\omega)$ with the bosonic thermal occupation number $n_{\text{th}}(\omega) = 1/(e^{\hbar\omega/k_B T} - 1)$. $J(\omega) = \pi \sum_v |\lambda_v|^2 \delta(\omega - \omega_v) \equiv \pi\alpha\omega/2$ is the phonon spectral density with the dissipation strength α and $J(-\omega) = -J(\omega)$.

3. Cavity response

Combined with input-output theory [55], the cavity transmission at frequency f_p yields

$$S_{21} = A e^{i\varphi} = \frac{i\sqrt{\kappa_1 \kappa_2}}{2\pi(f_c - f_p) + g^2 \chi(2\pi f_p) - i\kappa/2} + q. \tag{B7}$$

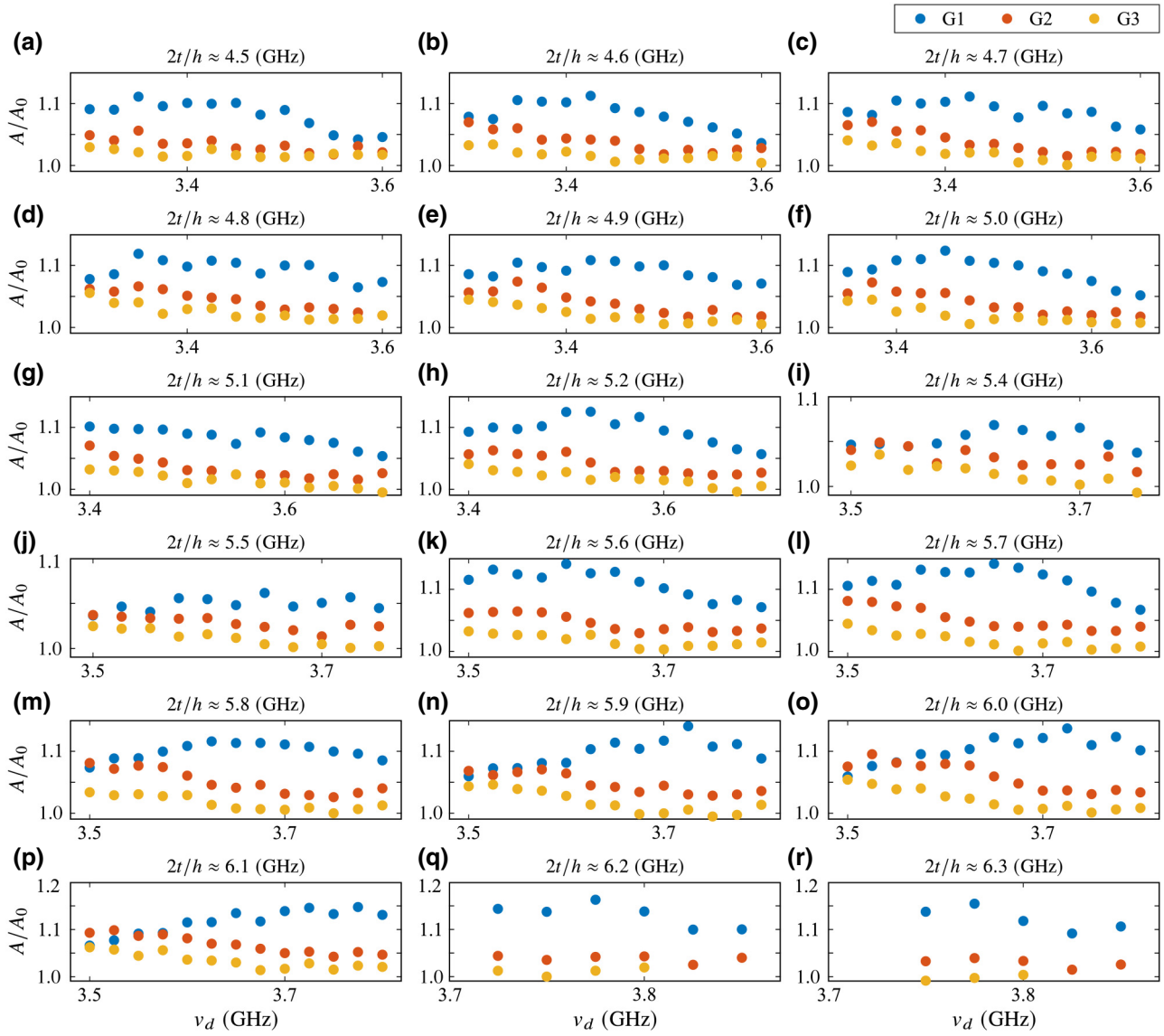

FIG. 6. The maximum A/A_0 at G1 (blue), G2 (red), and G3 (orange) extracted from LZSM patterns as a function of driving frequency v_d for different tunnel coupling $2t$. The data of $2t/h \approx 5.3$ GHz are shown in Fig. 3 in the main text.

A and φ are the amplitude and phase of S_{21}, respectively. And f_c (f_p) is the cavity (probe) frequency. g is the coupling strength between the DQD and the cavity. $\kappa = \kappa_1 + \kappa_2 + \kappa_{\text{int}}$ is the total decay rate of the cavity, where κ_1 (κ_2) is the decay rate of cavity port 1 (2) and κ_{int} is the internal decay rate of the cavity. We add a complex constant q to include the Fano effect due to interference between microwave transmission through the cavity and through a background [59]. In this experiment, we obtain the constant $q = 0 + 0.084i$ by fitting the bare cavity transmission. $A_0 = |-2\sqrt{\kappa_1\kappa_2}/\kappa + q|$ is the bare cavity transition amplitude with the DQD in the blockade regime at $f_p = f_c$. Then the normalized cavity amplitude is obtained with A/A_0.

The susceptibility χ for the DQD is a function of Floquet states,

$$\chi(2\pi f_p) = \sum_{\alpha,\beta,k} \frac{(p_\alpha - p_\beta)|Z_{\alpha\beta,k}|^2}{2\pi f_p + (\mu_\alpha - \mu_\beta)/\hbar - 2\pi k v_d + i\gamma/2}, \tag{B8}$$

where $Z_{\alpha\beta,k}$ is the kth Fourier component of the transition matrix element as $Z_{\alpha\beta,k} = \int_0^T dt/T e^{i2\pi k v_d t} \langle \phi_\alpha(t)|\sigma_z|\phi_\beta(t)\rangle$. γ is the decoherence rate between states of the DQD. As in the experiment, we focus on the region where detuning ϵ is near zero, we assume that γ will not change a lot, which leads to little variation in the normalized cavity

amplitude A/A_0. Therefore, we fix γ in all the theoretical simulations.

APPENDIX C: THE DEPENDENCE OF CAVITY GAIN ON TUNNEL COUPLING

Here we show the maximum cavity gain data measured at different tunnel coupling $2t$. At each $2t$, we change v_d and extract the gain at G1, G2, and G3. The complete experimental data are shown in Fig. 6. From this, the maximum cavity gain obtained at different $2t$ and the optimal driving frequency v_d^{opt} are determined and illustrated in Fig. 4 in the main text.

[1] Z.-L. Xiang, S. Ashhab, J. Q. You, and F. Nori, Hybrid quantum circuits: Superconducting circuits interacting with other quantum systems, Rev. Mod. Phys. **85**, 623 (2013).

[2] G. Burkard, M. J. Gullans, X. Mi, and J. R. Petta, Superconductor–semiconductor hybrid-circuit quantum electrodynamics, Nat. Rev. Phys. **2**, 129 (2020).

[3] A. Blais, A. L. Grimsmo, S. M. Girvin, and A. Wallraff, Circuit quantum electrodynamics, Rev. Mod. Phys. **93**, 025005 (2021).

[4] A. Wallraff, D. I. Schuster, A. Blais, L. Frunzio, R. S. Huang, J. Majer, S. Kumar, S. M. Girvin, and R. J. Schoelkopf, Strong coupling of a single photon to a superconducting qubit using circuit quantum electrodynamics, Nature **431**, 162 (2004).

[5] I. Chiorescu, P. Bertet, K. Semba, Y. Nakamura, C. J. P. M. Harmans, and J. E. Mooij, Coherent dynamics of a flux qubit coupled to a harmonic oscillator, Nature **431**, 159 (2004).

[6] J. J. Viennot, M. C. Dartiailh, A. Cottet, and T. Kontos, Coherent coupling of a single spin to microwave cavity photons, Science **349**, 408 (2015).

[7] A. Stockklauser, P. Scarlino, J. V. Koski, S. Gasparinetti, C. K. Andersen, C. Reichl, W. Wegscheider, T. Ihn, K. Ensslin, and A. Wallraff, Strong Coupling Cavity QED with Gate-Defined Double Quantum Dots Enabled by a High Impedance Resonator, Phys. Rev. X **7**, 011030 (2017).

[8] X. Mi, J. V. Cady, D. M. Zajac, P. W. Deelman, and J. R. Petta, Strong coupling of a single electron in silicon to a microwave photon, Science **355**, 156 (2017).

[9] N. Samkharadze, G. Zheng, N. Kalhor, D. Brousse, A. Sammak, U. C. Mendes, A. Blais, G. Scappucci, and L. M. K. Vandersypen, Strong spin-photon coupling in silicon, Science **359**, 1123 (2018).

[10] A. J. Landig, J. V. Koski, P. Scarlino, U. C. Mendes, A. Blais, C. Reichl, W. Wegscheider, A. Wallraff, K. Ensslin, and T. Ihn, Coherent spin–photon coupling using a resonant exchange qubit, Nature **560**, 179 (2018).

[11] X. Mi, M. Benito, S. Putz, D. M. Zajac, J. M. Taylor, G. Burkard, and J. R. Petta, A coherent spin–photon interface in silicon, Nature **555**, 599 (2018).

[12] B. Wang, T. Lin, H. Li, S. Gu, M. Chen, G. Guo, H. Jiang, X. Hu, G. Cao, and G. Guo, Correlated spectrum of distant semiconductor qubits coupled by microwave photons, Sci. Bull. **66**, 332 (2021).

[13] J. Majer, J. M. Chow, J. M. Gambetta, J. Koch, B. R. Johnson, J. A. Schreier, L. Frunzio, D. I. Schuster, A. A. Houck, A. Wallraff, A. Blais, M. H. Devoret, S. M. Girvin, and R. J. Schoelkopf, Coupling superconducting qubits via a cavity bus, Nature **449**, 443 (2007).

[14] M. A. Sillanpää, J. I. Park, and R. W. Simmonds, Coherent quantum state storage and transfer between two phase qubits via a resonant cavity, Nature **449**, 438 (2007).

[15] D. J. van Woerkom, P. Scarlino, J. H. Ungerer, C. Müller, J. V. Koski, A. J. Landig, C. Reichl, W. Wegscheider, T. Ihn, K. Ensslin, and A. Wallraff, Microwave Photon-Mediated Interactions between Semiconductor Qubits, Phys. Rev. X **8**, 041018 (2018).

[16] P. Scarlino, D. J. van Woerkom, U. C. Mendes, J. V. Koski, A. J. Landig, C. K. Andersen, S. Gasparinetti, C. Reichl, W. Wegscheider, K. Ensslin, T. Ihn, A. Blais, and A. Wallraff, Coherent microwave-photon-mediated coupling between a semiconductor and a superconducting qubit, Nat. Commun. **10**, 3011 (2019).

[17] A. J. Landig, J. V. Koski, P. Scarlino, C. Müller, J. C. Abadillo-Uriel, B. Kratochwil, C. Reichl, W. Wegscheider, S. N. Coppersmith, M. Friesen, A. Wallraff, T. Ihn, and K. Ensslin, Virtual-photon-mediated spin-qubit–transmon coupling, Nat. Commun. **10**, 5037 (2019).

[18] F. Borjans, X. G. Croot, X. Mi, M. J. Gullans, and J. R. Petta, Resonant microwave-mediated interactions between distant electron spins, Nature **577**, 195 (2020).

[19] P. Harvey-Collard, J. Dijkema, G. Zheng, A. Sammak, G. Scappucci, and L. M. K. Vandersypen, Coherent Spin-Spin Coupling Mediated by Virtual Microwave Photons, Phys. Rev. X **12**, 021026 (2022).

[20] G. Zheng, N. Samkharadze, M. L. Noordam, N. Kalhor, D. Brousse, A. Sammak, G. Scappucci, and L. M. K. Vandersypen, Rapid gate-based spin read-out in silicon using an on-chip resonator, Nat. Nanotechnol. **14**, 742 (2019).

[21] P. Scarlino, D. J. van Woerkom, A. Stockklauser, J. V. Koski, M. C. Collodo, S. Gasparinetti, C. Reichl, W. Wegscheider, T. Ihn, K. Ensslin, and A. Wallraff, All-Microwave Control and Dispersive Readout of Gate-Defined Quantum Dot Qubits in Circuit Quantum Electrodynamics, Phys. Rev. Lett. **122**, 206802 (2019).

[22] H. J. Kimble, The quantum internet, Nature **453**, 1023 (2008).

[23] A. Blais, R.-S. Huang, A. Wallraff, S. M. Girvin, and R. J. Schoelkopf, Cavity quantum electrodynamics for superconducting electrical circuits: An architecture for quantum computation, Phys. Rev. A **69**, 062320 (2004).

[24] X. Gu, A. F. Kockum, A. Miranowicz, Y.-x. Liu, and F. Nori, Microwave photonics with superconducting quantum circuits, Phys. Rep. **718-719**, 1 (2017).

[25] J. R. Petta, A. C. Johnson, C. M. Marcus, M. P. Hanson, and A. C. Gossard, Manipulation of a Single Charge in a Double Quantum Dot, Phys. Rev. Lett. **93**, 186802 (2004).

[26] H. G. J. Eenink, L. Petit, W. I. L. Lawrie, J. S. Clarke, L. M. K. Vandersypen, and M. Veldhorst, Tunable coupling and isolation of single electrons in silicon metal-oxide-semiconductor quantum dots, Nano Lett. **19**, 8653 (2019).

[27] X. Mi, C. G. Péterfalvi, G. Burkard, and J. R. Petta, High-Resolution Valley Spectroscopy of Si Quantum Dots, Phys. Rev. Lett. **119**, 176803 (2017).

[28] T. R. Hartke, Y.-Y. Y. Liu, M. J. Gullans, and J. R. Petta, Microwave Detection of Electron-Phonon Interactions in a Cavity-Coupled Double Quantum Dot, Phys. Rev. Lett. **120**, 097701 (2018).

[29] A. J. Landig, J. V. Koski, P. Scarlino, C. Reichl, W. Wegscheider, A. Wallraff, K. Ensslin, and T. Ihn, Microwave-Cavity-Detected Spin Blockade in a Few-Electron Double Quantum Dot, Phys. Rev. Lett. **122**, 213601 (2019).

[30] Y.-Y. Liu, K. D. Petersson, J. Stehlik, J. M. Taylor, and J. R. Petta, Photon Emission from a Cavity-Coupled Double Quantum Dot, Phys. Rev. Lett. **113**, 036801 (2014).

[31] Y.-Y. Liu, J. Stehlik, C. Eichler, M. J. Gullans, J. M. Taylor, and J. R. Petta, Semiconductor double quantum dot micromaser, Science **347**, 285 (2015).

[32] Y.-Y. Liu, J. Stehlik, C. Eichler, X. Mi, T. R. Hartke, M. J. Gullans, J. M. Taylor, and J. R. Petta, Threshold Dynamics of a Semiconductor Single Atom Maser, Phys. Rev. Lett. **119**, 097702 (2017).

[33] J. Stehlik, Y.-Y. Liu, C. Eichler, T. R. Hartke, X. Mi, M. J. Gullans, J. M. Taylor, and J. R. Petta, Double Quantum Dot Floquet Gain Medium, Phys. Rev. X **6**, 041027 (2016).

[34] M.-B. Chen, B.-C. Wang, S.-S. Gu, T. Lin, H.-O. Li, G. Cao, and G.-P. Guo, Micro-scale photon source in a hybrid cQED system, Chinese Phys. B **30**, 048507 (2021).

[35] A. Stockklauser, V. F. Maisi, J. Basset, K. Cujia, C. Reichl, W. Wegscheider, T. Ihn, A. Wallraff, and K. Ensslin, Microwave Emission from Hybridized States in a Semiconductor Charge Qubit, Phys. Rev. Lett. **115**, 046802 (2015).

[36] S. Shevchenko, S. Ashhab, and F. Nori, Landau–Zener–Stückelberg interferometry, Phys. Rep. **492**, 1 (2010).

[37] M. J. Gullans, J. Stehlik, Y.-Y. Liu, C. Eichler, J. R. Petta, and J. M. Taylor, Sisyphus Thermalization of Photons in a Cavity-Coupled Double Quantum Dot, Phys. Rev. Lett. **117**, 056801 (2016).

[38] J. V. Koski, A. J. Landig, A. Pályi, P. Scarlino, C. Reichl, W. Wegscheider, G. Burkard, A. Wallraff, K. Ensslin, and T. Ihn, Floquet Spectroscopy of a Strongly Driven Quantum Dot Charge Qubit with a Microwave Resonator, Phys. Rev. Lett. **121**, 043603 (2018).

[39] M.-B. Chen, S.-L. Jiang, N. Wang, B.-C. Wang, T. Lin, S.-S. Gu, H.-O. Li, G. Cao, and G.-P. Guo, Microwave-Resonator-Detected Excited-State Spectroscopy of a Double Quantum Dot, Phys. Rev. Appl. **15**, 044045 (2021).

[40] K. D. Petersson, L. W. McFaul, M. D. Schroer, M. Jung, J. M. Taylor, A. A. Houck, and J. R. Petta, Circuit quantum electrodynamics with a spin qubit, Nature **490**, 380 (2012).

[41] X. Mi, S. Kohler, and J. R. Petta, Landau-Zener interferometry of valley-orbit states in Si/SiGe double quantum dots, Phys. Rev. B **98**, 161404 (2018).

[42] M.-B. Chen, B.-C. Wang, S. Kohler, Y. Kang, T. Lin, S.-S. Gu, H.-O. Li, G.-C. Guo, X. Hu, H.-W. Jiang, G. Cao, and G.-P. Guo, Floquet state depletion in ac-driven circuit QED, Phys. Rev. B **103**, 205428 (2021).

[43] J. H. Shirley, Solution of the Schrödinger equation with a Hamiltonian periodic in time, Phys. Rev. **138**, B979 (1965).

[44] P. S. Mundada, A. Gyenis, Z. Huang, J. Koch, and A. A. Houck, Floquet-Engineered Enhancement of Coherence Times in a Driven Fluxonium Qubit, Phys. Rev. Appl. **14**, 054033 (2020).

[45] K. R. Amin, C. Ladner, G. Jourdan, S. Hentz, N. Roch, and J. Renard, Loss mechanisms in TiN high impedance superconducting microwave circuits, Appl. Phys. Lett. **120**, 164001 (2022).

[46] H. Rotzinger, S. T. Skacel, M. Pfirrmann, J. N. Voss, J. Münzberg, S. Probst, P. Bushev, M. P. Weides, A. V. Ustinov, and J. E. Mooij, Aluminium-oxide wires for superconducting high kinetic inductance circuits, Supercond. Sci. Technol. **30**, 025002 (2017).

[47] L. Grünhaupt, N. Maleeva, S. T. Skacel, M. Calvo, F. Levy-Bertrand, A. V. Ustinov, H. Rotzinger, A. Monfardini, G. Catelani, and I. M. Pop, Loss Mechanisms and Quasiparticle Dynamics in Superconducting Microwave Resonators Made of Thin-Film Granular Aluminum, Phys. Rev. Lett. **121**, 117001 (2018).

[48] X. Mi, J. V. Cady, D. M. Zajac, J. Stehlik, L. F. Edge, and J. R. Petta, Circuit quantum electrodynamics architecture for gate-defined quantum dots in silicon, Appl. Phys. Lett. **110**, 043502 (2017).

[49] N. Holman, J. P. Dodson, L. F. Edge, S. N. Coppersmith, M. Friesen, R. McDermott, and M. A. Eriksson, Microwave engineering for semiconductor quantum dots in a cQED architecture, Appl. Phys. Lett. **117**, 083502 (2020).

[50] P. Harvey-Collard, G. Zheng, J. Dijkema, N. Samkharadze, A. Sammak, G. Scappucci, and L. M. K. Vandersypen, On-Chip Microwave Filters for High-Impedance Resonators with Gate-Defined Quantum Dots, Phys. Rev. Appl. **14**, 034025 (2020).

[51] N. Holman, D. Rosenberg, D. Yost, J. L. Yoder, R. Das, W. D. Oliver, R. McDermott, and M. A. Eriksson, 3D integration and measurement of a semiconductor double quantum dot with a high-impedance TiN resonator, npj Quantum Inf. **7**, 137 (2021).

[52] D. Bozyigit, C. Lang, L. Steffen, J. M. Fink, C. Eichler, M. Baur, R. Bianchetti, P. J. Leek, S. Filipp, M. P. da Silva, A. Blais, and A. Wallraff, Antibunching of microwave-frequency photons observed in correlation measurements using linear detectors, Nat. Phys. **7**, 154 (2011).

[53] M. P. da Silva, D. Bozyigit, A. Wallraff, and A. Blais, Schemes for the observation of photon correlation functions in circuit QED with linear detectors, Phys. Rev. A **82**, 043804 (2010).

[54] Y.-Y. Liu, J. Stehlik, X. Mi, T. R. Hartke, M. J. Gullans, and J. R. Petta, On-Chip Quantum-Dot Light Source for Quantum-Device Readout, Phys. Rev. Appl. **9**, 014030 (2018).

[55] S. Kohler, Dispersive readout: Universal theory beyond the rotating-wave approximation, Phys. Rev. A **98**, 023849 (2018).

[56] M. Silveri, J. Tuorila, M. Kemppainen, and E. Thuneberg, Probe spectroscopy of quasienergy states, Phys. Rev. B **87**, 134505 (2013).

[57] S. Kohler, T. Dittrich, and P. Hänggi, Floquet-Markovian description of the parametrically driven, dissipative harmonic quantum oscillator, Phys. Rev. E **55**, 300 (1997).

[58] F. Forster, G. Petersen, S. Manus, P. Hänggi, D. Schuh, W. Wegscheider, S. Kohler, and S. Ludwig, Characterization of Qubit Dephasing by Landau-Zener-Stückelberg-Majorana Interferometry, Phys. Rev. Lett. **112**, 116803 (2014).

[59] J. Leppäkangas, J. D. Brehm, P. Yang, L. Guo, M. Marthaler, A. V. Ustinov, and M. Weides, Resonance inversion in a superconducting cavity coupled to artificial atoms and a microwave background, Phys. Rev. A **99**, 063804 (2019).